Available online at www.sciencedirect.com
ScienceDirect
Geochimica et Cosmochimica Acta 72 (2008) 4627–4641
Geochimica et Cosmochimica Acta
www.elsevier.com/locate/gca

Carbon solubility in core melts in a shallow magma ocean environment and distribution of carbon between the Earth's core and the mantle

Rajdeep Dasgupta *, David Walker

Lamont-Doherty Earth Observatory, Columbia University, P.O. Box 1000, 61 Route 9W, Palisades, NY 10964-8000, USA

Received 28 March 2008; accepted in revised form 24 June 2008; available online 8 July 2008

Abstract

The solubility of carbon in Fe and Fe–5.2 wt.% Ni melts, saturated with graphite, determined by electron microprobe analysis of quenched metal melts was 5.8 ± 0.1 wt.% at 2000 °C, 6.7 ± 0.2 wt.% at 2200 °C, and 7.4 ± 0.2 wt.% at 2410 °C at 2 GPa, conditions relevant for core/mantle differentiation in a shallow magma ocean. These solubilities are slightly lower than low-pressure literature values and significantly beneath calculated values for even higher pressures [e.g., Wood B. J. (1993) Carbon in the core. *Earth Planet. Sci. Lett.* **117**, 593–607]. The trend of C solubility versus temperature for Fe–5.2 wt.% Ni melt, within analytical uncertainties, is similar to or slightly lower (~0.2–0.4 wt.%) than that of pure Fe. Carbon content of core melts and residual mantle silicates derived from equilibrium batch or fractional segregation of core liquids and their comparison with our solubility data and carbon content estimate of the present day mantle, respectively, constrain the partition coefficient of carbon between silicate and metallic melts, $D_C^{silicate/metal}$ in a magma ocean. For the entire range of possible bulk Earth carbon content from chondritic to subchondritic values, $D_C^{silicate/metal}$ of 10^{-4} to 1 is derived. But for ~1000 ppm bulk Earth carbon, $D_C^{silicate/metal}$ is between 10^{-2} and 1. Using the complete range of possible $D_C^{silicate/metal}$ for a magma ocean at ~2200 °C, we predict maximum carbon content of the Earth's core to be ~6–7 wt.% and a preferred value of 0.25 ± 0.15 wt.% for a bulk Earth carbon concentration of ~1000 ppm.

1. INTRODUCTION

The exchange of carbon between different terrestrial reservoirs is an important step in the global carbon cycle, and has a key influence on the habitability of our planet. Though the term 'carbon cycle' mostly refers to exchange of the volatile species between the near-surface reservoirs such as atmosphere and biosphere, oceans, and soils that operates on human time scales (Berner, 1999), the Earth's interior is thought to be the largest reservoir for terrestrial carbon (Javoy et al., 1982; Javoy, 1997). The knowledge of carbon content of various deep Earth reservoirs is important as carbon affects the melting phase relations of mantle rocks (Wyllie and Huang, 1975; Dasgupta and Hirschmann, 2006) and core metal (Wood, 1993), influences the physical properties such as densities and viscosities of molten silicates (Lange, 1994; Bourgue and Richet, 2001) and metals (Poirier, 1994), acts as an agent of mass transfer in the form of very mobile carbonate-rich melts (Hunter and McKenzie, 1989; Minarik and Watson, 1995), and also has significant impact on partitioning of other key elements between minerals and melts or two immiscible melts in both silicate–carbonate (Blundy and Dalton, 2000) and in metal systems (Jana and Walker, 1997; Chabot et al., 2006). But the carbon budget of the Earth and concentrations of carbon in various deep Earth reservoirs are poorly constrained.

Although there is little doubt that the total estimated mass of carbon in the Earth's interior is by far the largest reservoir (Javoy et al., 1982; Marty and Jambon, 1987; Zhang and Zindler, 1993; Sleep and Zahnle, 2001), its

* Corresponding author. Present address: Department of Earth Science, Rice University, Houston, Texas, USA. Fax: +1 713 348 5214.
E-mail address: Rajdeep.Dasgupta@rice.edu (R. Dasgupta).

0016-7037/$ - see front matter © 2008 Elsevier Ltd. All rights reserved.
doi:10.1016/j.gca.2008.06.023

relative distribution between the metallic core and the silicate mantle is uncertain. On one hand, models of the whole Earth carbon cycle estimate mantle carbon mass of ~0.8–40×10^{23} g and do not include the core as a potential carbon reservoir (Sleep and Zahnle, 2001; Coltice et al., 2004), on the other, carbon is proposed to be one of the light alloying elements in the Earth's core (Wood, 1993; Poirier, 1994; Li and Fei, 2003; Huang et al., 2005), with proposed concentration as high as ~4 wt.% (Hillgren et al., 2000)—i.e., $\sim 7.8 \times 10^{25}$ g of C or as much as 2–3 orders of magnitude higher than that of the Earth's mantle. Furthermore, the lowest estimated concentration in the core is as low as 0.2 wt.% (McDonough, 2003). If carbon is the dominant light element in the core, then the core would have orders of magnitude higher carbon budget than the mantle, but if it is a minor light element component, then the core's contribution to the total terrestrial carbon budget can be comparable or smaller than that of the mantle.

The uncertainty in the relative distribution of carbon between metal and silicate Earth arises due to lack of constraints on the solubility limit of carbon in metallic melts and on partitioning behavior of carbon between the metal and the silicate during core formation. To date many high pressure, high temperature experiments on trace element partitioning between metallic melt and silicate melt have been performed in graphite capsules (Thibault and Walter, 1995; Walter and Thibault, 1995; Jana and Walker, 1997; Righter et al., 1997; Jana and Walker, 1999; Righter and Drake, 2000; Li and Agee, 2001b; Li and Agee, 2001a; Chabot and Agee, 2003; Righter and Shearer, 2003; Chabot et al., 2005). Thus one may expect that there should not be dearth of experimental data on equilibrium partitioning of carbon between metallic and silicate melts. However, perhaps owing to analytical difficulty, none of these studies made attempts to actually measure carbon content in both of the immiscible melts, and hence no experimental data on carbon partitioning between metal and silicate melts in a magma ocean environment can be constrained from these studies. Based on thermodynamic models of gas solubilities in silicate and metallic melts, Kuramoto and Matsui (1996) and Kuramoto (1997) predict effectively zero partitioning of carbon to silicate melt during metal–silicate equilibration in a magma ocean, i.e., complete partitioning of protoearth carbon to the core. If this is true then the carbon in the mantle source regions of mid-ocean ridge and ocean island basalts, which ranges from ~50 to 1000 ppm (Javoy and Pineau, 1991; Dixon et al., 1997; Marty and Tolstikhin, 1998; Saal et al., 2002; Pineau et al., 2004), cannot be explained by a mantle that crystallizes largely from the silicate melt residual to core separation and needs to come entirely from 'late veneer'.

While experimental metal–silicate carbon partitioning data are completely lacking, some constraints on high pressure carbon solubility limit in metallic melt exist in the literature. Current opinion about carbon dissolution into molten Fe at high pressures comes from the experiments and thermodynamic calculation of Wood (1993), which build on one-atmosphere steel industry data on the Fe–C–S system summarized in Shunk (1969), Chipman (1972), and after Wang et al. (1991). Although the synthesis of Wood (1993) provides the baseline for our understanding regarding carbon in metallic Fe-rich molten alloy, the actual measurements (gravimetric analysis: Wang et al., 1991; electron probe analysis: Wood, 1993) of carbon solubility in molten Fe to support the constructed high pressure Fe–C phase diagram, particularly the graphite saturated liquidus, do not go beyond 1600 °C. The higher temperature one atmosphere carbon solubility data reported in Shunk (1969) and Chipman (1972) largely come from the work of Cahil et al. (1964), which reports graphite saturated experiments to 2875 °C but only measured the Fe and reported the C by difference. In addition to the Fe–C ± S phase equilibria synthesis of Wood (1993), Righter et al. (1997) and Righter and Drake (2000) attempted microprobe analysis of carbon for their immiscible metallic melts in graphite saturated runs, using carbon coated samples and standards. At 7 GPa and 1650–1750 °C, Righter et al. (1997) reports a carbon solubility of 4.2–4.7 wt.% for their molten Fe-rich alloy with 7.5–10.0 wt.% Ni. Similarly, Righter and Drake (2000) reported carbon content of 2.9 wt.% at the same pressure and at 1750 °C for a molten alloy with 51.5 wt.% Fe, 26.2 wt.% Ni, and 16.3 wt.% Co. These estimates are distinctly lower than the carbon solubility prediction of Wood (1993) at similar pressures (at 5 GPa and 1750 °C that the carbon content of graphite saturated molten Fe is ~6.5 wt.%). If the measurements of Righter et al. (1997) and Righter and Drake (2000) are appropriate then the calculated phase diagram of Wood (1993) might be in error or there might be a strong negative dependence of carbon solubility on Ni and Co content of the molten alloy. Holzheid and Grove (2005) also estimated carbon content of quenched Fe–Ni–C melt, in equilibrium with olivine and saturated in graphite/diamond, for some of their experimental charges. They estimated carbon solubility of 2.8–3.5 wt.% for an Fe-rich molten alloy with 8–10 wt.% Ni at ~2.2 GPa and 1500 °C. Their (Holzheid and Grove, 2005) measurements also indicate distinctly lower carbon solubility (0.91 wt.% lower) in molten Fe with respect to the available one-atmosphere data. Therefore, significant uncertainty remains on high pressure solubility limit of carbon for core-like metallic melt, especially at temperatures relevant for a magma ocean environment ($T > 1700$ °C). Thus a systematic study at high pressure and especially to high temperature is needed to constrain the carbon solubility in Fe and Fe–Ni core melt.

To determine the storage capacity of carbon in the core and to constrain the partitioning of carbon between metal and silicate, in this study we have measured the solubility of carbon in molten Fe and Fe–5.2 wt.% Ni alloy at pressure–temperature conditions relevant for a shallow magma ocean. Experiments were performed at 2 GPa and to temperatures up to 2500 °C. Comparison of our solubility data and the observed concentration of carbon in the mantle with the model carbon concentration in silicate and metal, assuming the core to be equilibrium batch or fractional melt of the protoearth, constrain the plausible values for carbon partition coefficient between silicate and metallic melts. From the range of plausible carbon partition coefficients between metal and silicate, we put constraints on the carbon content of the Earth's core.

2. EXPERIMENTAL APPROACH

2.1. Methods

Experiments were performed at 2 GPa using an end-loaded piston cylinder apparatus. To cover the experimental temperature range from 1200 to 2500 °C, four different half-inch assemblies with $BaCO_3$ pressure cell were used (Fig. 1). Experiments between 1200 and 1600 °C were conducted using $BaCO_3$ pressure cell of 1/2″ outer diameter (OD) and 5/16″ inner diameter (ID), MgO spacers, and Al_2O_3 sleeve to separate the capsule and thermocouple from the rest of the assembly (Fig. 1a). The runs above 1600 °C typically employed a Ca^{2+} doped $LaCrO_3$ insulator sleeve (3/8″ OD, 1/5″ ID) to separate the graphite heater (1/5″ OD, 1/8″ ID) from the $BaCO_3$ pressure cell (1/2″ OD, 3/8″ ID) (Fig. 1b and c). Experiments above 1800 °C were conducted following the assembly of Cottrell and Walker (2006), with graphite furnace cut short in length to 1″ to reduce heat loss to the piston and base plug: 1/8″ long MgO end plugs wrapped in 0.001″ thick Mo foil were used to complete the heater circuit (Fig. 1c). All the spacers, the 4-bore thermocouple sleeve, and the sleeve around the capsule were made of crushable MgO in this assembly. Intermediate temperature runs between 1600 and 1800 °C were conducted by slightly modifying the assembly design of Cottrell and Walker (2006). In these runs, the graphite heater was cut short to 1.125″ and 1/8″ thick graphite disk completes the circuit at the bottom end of the heater (Fig. 1b). All the spacers, the sleeve to separate the capsule from the heater, and the 4-bore thermocouple sleeve for this assembly were made of Al_2O_3 (Fig. 1b). To achieve faster quench and thus to avoid any quench modifications of metallic melt compositions, additional experiments above 2000 °C were carried out using an MgO insulator sleeve (5/16″ OD, 11/64″ ID) to separate the graphite heater (11/64″ OD, 1/8″ ID) from the $BaCO_3$ pressure cell (1/2″ OD, 5/16″ ID, 1.312″ long) (Fig. 1d). All four assemblies were wrapped with Pb foil, in order to lubricate the pressure vessel bore and to contain the friable $BaCO_3$ cell.

Two different starting materials were investigated—(1) pure Fe (99.995% Fe wire from Alfa-Aesar) and (2) Fe–5.2 wt.% Ni mix (99.9% Fe powder from Alfa-Aesar and 99.9% pure Ni powder from Fisher Scientific). Samples were contained in graphite capsules to achieve carbon saturation and temperature during the experiments was monitored by type-D ($W_{97}Re_3/W_{75}Re_{25}$) thermocouples. All the assemblies were compressed to the run pressure of 2 GPa using the cold piston-in technique. In order to reduce porosity in the graphite capsules before the formation of metallic melts, experiments were held at 900–1000 °C for 12–24 h. After sintering, the experiments were heated typically at an average rate of 50 °C/min. The high-temperature runs (>1600 °C) with thin-walled $BaCO_3$ cell were held at 1400 °C for 15 min before quickly ramping to the run temperature. The duration at nominal run temperature varied between 72 h and 10 s (Table 1). All runs were quenched by turning off the heater power. Pressure calibrations for thick and thin walled $BaCO_3$ assemblies were based on Fram and Longhi (1992), and temperature correction to account for the difference in location between the thermocouple junctions and the sample hotspot was after Longhi (2005).

At the end of each experiment, the entire assembly was embedded in epoxy and ground longitudinally to expose the medial section of the sample. Coarse sample grinding was done using a silicon carbide strip grinder and fine polishing with 0.3 μm Al_2O_3 powder on a lapidary wheel using water as lubricant. After a desirable polished surface was achieved, samples were cleaned in an ultrasonic bath and

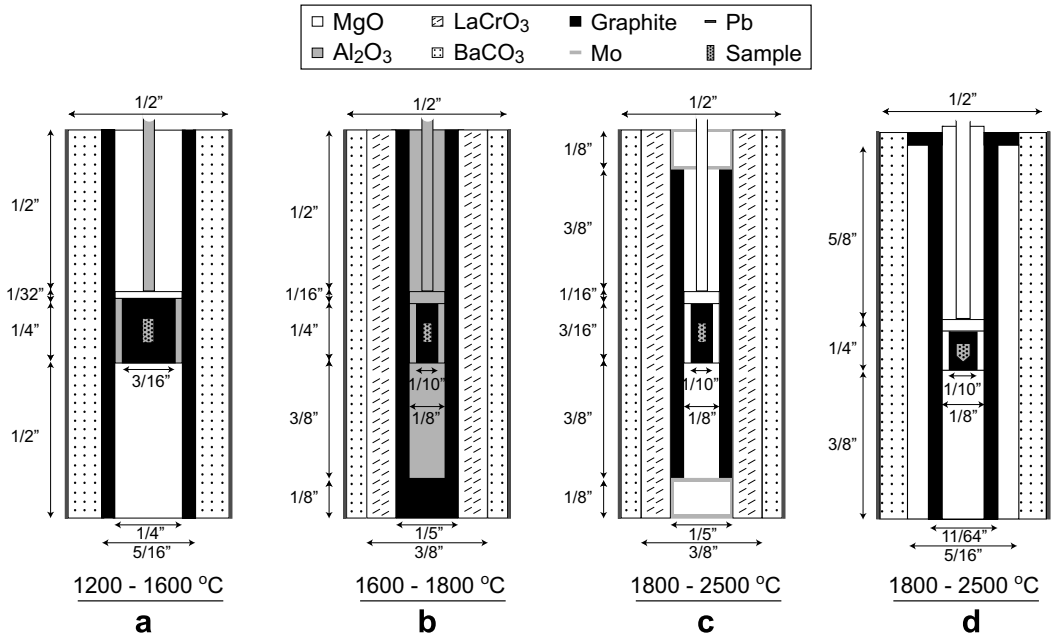

Fig. 1. Piston cylinder assemblies used in this study to cover the temperature range between 1200 and 2500 °C.

Table 1
Run conditions and melt compositions from 2 GPa graphite saturated experiments of Fe–C binary and Fe–5.2% Ni–C pseudo binary

Run#	T (°C)	Duration[a]	Phase[b]	n[c]	Fe	Ni	C	Sum
Fe–C binary								
RD 3.6	1250	72 h	Cementite	20	93.77(0.05)[d]		6.5	100.26
RD 3.11	1275	24 h	Cementite	17	93.73(0.05)		6.9	100.64
			Melt	20	94.68(0.09)		5.7	100.38
RD 3.2	1300	69 h	Melt	9	94.13(0.23)		5.5(0.2)	99.62
RD 3.8	1400	26 h	Melt	10	94.20(0.09)		5.4(0.1)	99.61
RD 3.9	1500	90 min	Melt	12	94.19(0.29)		5.6(0.2)	99.75
RD 3.10	1600	60 min	Melt	14	94.22(0.26)		5.5(0.3)	99.69
RD 3.12	1700	100 min	Melt	15	94.67(0.18)		5.6(0.1)	100.28
RD 3.13a	2000	10 s	Melt	10	94.42(0.10)		5.8(0.2)	100.21
RD 3.13b	2000	0.5 min	Melt	16	94.13(0.07)		5.9(0.1)	100.04
RD 3.13c	2000	1 min	Melt	14	94.47(0.16)		5.8(0.1)	100.23
RD 3.13	2000	5 min	Melt	13	93.97(0.07)		5.8(0.1)	99.79
GG995[e]	2200	4 min	Melt	10	93.47(0.13)		6.7(0.2)	100.12
RD 3.19	2250	10 min	Melt	18	93.20(0.15)		6.5(0.2)	99.70
GG994	2350	10 s	Melt	11	93.19(0.12)		7.1(0.2)	100.31
GG996	2410	10 min	Melt	6	92.76(0.13)		7.4(0.2)	100.20
RD 3.17	2500	5 min	Melt	12	92.70(0.25)		7.5(0.4)	100.20
Fe–5.2 wt.% Ni–C pseudo binary								
RD 3.15	1600	2 h	Melt	11	89.68(0.05)	5.13(0.08)	5.4(0.1)	100.21
RD 3.16	1800	30 min	Melt	14	89.49(0.16)	4.78(0.08)	5.6(0.2)	99.87
RD 3.18	2000	15 min	Melt	18	89.44(0.14)	4.68(0.15)	5.7(0.3)	99.77
RD 3.20	2200	4 min	Melt	12	88.89(0.29)	5.00(0.18)	6.2(0.5)	100.12
RD 3.21	2400	10 min	Melt	10	88.16(0.31)	4.87(0.04)	7.0(0.3)	100.03

[a] All the runs were kept at 900–1000 °C for 12–24 h before subjecting them to the run temperature.
[b] All the runs are graphite saturated.
[c] Number of analyses averaged.
[d] Numbers in parentheses indicate standard error of the mean based on replicate analyses ($\sigma_M = \sigma/\sqrt{n}$). The errors in the carbon concentrations do not include the uncertainties owing to the instrumental blank value of carbon, which is ~0.5 wt.%.
[e] Run numbers with prefix GG are performed in the assembly with MgO insulating sleeve (Fig. 1d), which is likely to provide a more rapid quench in the high temperature solid media piston cylinder device. The temperature in the run GG995 was very unstable thus the reported nominal temperature should be taken as an estimate.

coated with Al along with standards for characterization using electron microprobe.

2.2. Attainment of equilibrium

The maximum durations of our experiments varied inversely with nominal run temperatures, with experiments ⩾2000 °C lasting 10 s–15 min. The run durations of our high temperature (⩾2000 °C) experiments are similar to the previous metal melt-silicate melt partitioning experiments performed at similar temperatures (Li and Agee, 1996, 2001a,b; Chabot and Agee, 2003; Chabot et al., 2005). Although our experiments were not reversed, attainment of equilibrium can be argued based on the following set of reasons. (a) A time series at 2000 °C and 2 GPa, for the graphite saturated Fe–C binary produced no discernible difference in the carbon content of the quenched melt for runs varying from 10 s to 5 min in duration (Fig. 2 and Table 1). This is consistent with the time series and chemical reversal experiments by Thibault and Walter (1995), which demonstrated that liquid state metal–silicate experiments at 5 GPa and ~2000 °C takes no more than 5 s to reach equilibrium, thus lending confidence to the choice of our run durations. More specifically, diffusion of C in Fe_3C liquid is known to be extremely fast and at ~2000 °C and 8 GPa a completely flat diffusion profile is expected for runs lasting only a few seconds (Dobson and Wiedenbeck, 2002). (b) X-ray intensity maps for Fe and C revealed no zonation

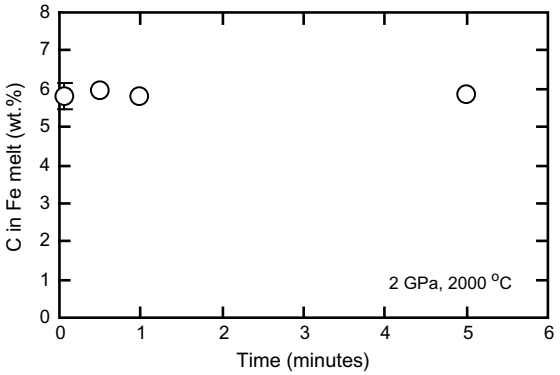

Fig. 2. Time series experiments performed at 2 GPa and 2000 °C for carbon incorporation into metallic Fe liquid. No discernible difference in the carbon content of the metallic Fe liquid with time indicates that the saturation value of carbon in liquid Fe metal is reached in less than 10 s. The error bars are standard error of the mean based on replicate analyses and the absence of an error bar indicates that it is smaller than the size of the symbol.

in terms of population of various quenched crystals across the capsule walls in our charges.

3. ANALYTICAL PROCEDURE

Run products were analyzed using a Cameca SX100 electron probe microanalyzer (EPMA) at the American Museum of Natural History. For WDS analysis of carbon, a Ni/C multilayer crystal (LPC2: large PC2 with $2d = 9.5$ nm and elemental range of B Kα to O Kα) was used. The samples and the standards were Al coated together for each run to keep X-ray absorptions uniform. One of the major problems in carbon measurements by EPMA is the sample surface contamination by carbon due to deposition of residual organic molecules at the point of electron beam impact. These organic molecules come from the vacuum greases, the residual oil vapors of the diffusion pump oil, and the contamination of the specimen itself (Robaut et al., 2006). Use of a cold finger and especially a low-pressure air or oxygen jet onto the sample surface, has been shown to be an effective way in minimizing carbon contamination (Bastin and Heijligers, 1986; Robaut et al., 2006), however, due to unavailability of either of those features in our electron probe, no such attempt to minimize carbon contamination could be made. For quantitative WDS analysis of crystalline metal carbides and quenched metallic melt, a fully focused and a 50–100 μm beam were used, respectively. For X-ray maps, a fully focused beam was used.

3.1. Choice of analytical standards

Cementite (Fe_3C: 6.67 wt.% C) was used as the primary standard for carbon, whereas Fe_7C_3 (8.43 wt.% C), glassy carbon (100 wt.% C), moissanite (SiC: 29.96 wt.% C), and a NIST standard 663 (0.57 wt.% C) served as secondary standards (Table 2). Our choice of cementite as the primary standard, over other commonly used carbon standards such as diamond, graphite, glassy carbon, and various carbon bearing steels, has the following advantages. (1) Difference in the chemical bonding between standards and unknowns are known to cause significant wavelength shifts or peak shape alteration for X-ray intensities of C Kα line (Bastin and Heijligers, 1986). But, the use of cementite as the primary standard made the requirement of area-peak-factor (APF) corrections unnecessary, as our unknown samples were either crystalline iron carbide or quenched aggregate of Fe ± Ni–C phases (see Section 4 for details). (2) The expected count rate for carbon is more or less comparable to that expected for the run products, which is mostly Fe/Fe–Ni carbide or their quenched aggregate. Thus, the unwanted interference of higher order Fe and Ni lines could easily be minimized by choosing a narrow window for the pulse-height-analyzer (PHA), without running the risk of pulse-shifts (a phenomenon observed when there is a large difference in count rates between the standard and the sample). (3) Use of Fe_3C as a standard also helped to avoid the interference of higher order metal lines such as Cr and Mn that are commonly present in commercial steel standards for carbon.

The standard cementite (Fe_3C) was synthesized in a piston cylinder apparatus at 2 GPa and 1200 °C using a 1/2″ assembly with $BaCO_3$ pressure cell, crushable MgO spacers, and graphite furnace. Two different synthesis approaches were used (Table 2)—(a) Fe and diamond powder mixed in stoichiometric proportion (6.67 wt.% C) under ethanol and run in a crushable MgO capsule for 67 h and (b) a pure Fe wire run in presence of excess carbon, i.e., loaded in a graphite capsule (Fig. 1a), following the suggested method of Tsuzuki et al. (1984) for 51 h. Fe_7C_3 was synthesized in a Walker-style multi anvil device at 7 GPa and 1350 °C using 8 mm truncation edge length WC cubes and a castable MgO octahedral assembly with $LaCrO_3$ heater and MgO spacers. A pure Fe wire run in presence of excess carbon, i.e., loaded in a graphite capsule, was used as the starting material. For the 7-h multi anvil run, temperature was monitored with a type-D thermocouple. To check the structure (and by implication the stoichiometry) of the targeted Fe_3C and Fe_7C_3, XRD spectra were collected from polished surfaces of the run products using Rigaku DMAX/RAPID Micro X-ray diffraction system at the American Museum of Natural History. The obtained spectra for the experimental

Table 2
Primary and secondary standards used for C analysis by electron probe

Standard	Synthesis condition/source					C (wt.%)	Comments[b]
	Run#[a]	P (GPa)	T (°C)	Duration (h)	Capsule		
Fe (99.995%)			Alfa-Aesar			0.00	Manufacturer
Low-C steel			NIST 663[c]			0.57	Manufacturer
Fe_3C[d]	RD 3.7	2	1200	67	MgO	6.67	Stoichiometry
Fe_3C[d]	RD 3.5	2	1200	51	Graphite	6.67	Stoichiometry
Fe_7C_3	BB893	7	1350	7	Graphite	8.43	Stoichiometry
SiC			AMNH mineral collection			29.96	Stoichiometry
Glassy C			Alfa-Aesar			100.00	Manufacturer

[a] Runs RD 3.7 and RD 3.5 are performed in an end-loaded piston cylinder and BB893 in a Walker-style multianvil (see text for further experimental details).
[b] Carbon concentration source—either manufacturer provided value or by stoichiometry, based on crystal structure confirmation by micro-XRD.
[c] NIST 663 contains 94.4 wt.% Fe, 0.32 wt.% Ni, 1.31 wt.% Cr, 1.50 wt.% Mn, 0.31 wt.% V, 0.74 wt.% Si, and 0.24 wt.% Al.
[d] Primary standards used for CKα calibration.

products from both the carbide standards were in agreement with previously published spectra. C Kα maps of the standards also showed no signs of heterogeneity except for small proportions of dispersed grains of ferropericlase for the Fe_3C standard synthesized in MgO capsule. Fe and Ni metal were used as standards for Fe and Ni, respectively. The Fe standard also served the purpose for measuring the blank for carbon at the peak position of C Kα.

3.2. Operating conditions

To achieve the optimum signal to noise ratio for carbon measurement, we varied the accelerating voltage, emission current of the electron beam, and the C Kα counting time. All the tests were performed with a defocused beam of 50 μm diameter and on our cementite standard.

3.2.1. Voltage and current optimization

We noticed that voltage of 9–13 kV and emission current of 70–100 nA produced the most stable and high peak:background ratio for C Kα (Fig. 3a). Higher accelerating voltage caused the peak:background ratio to decrease, possibly in part due to higher noise and due to production of C Kα X-rays too deep within the sample to escape without being absorbed. A slight but observable improvement of the peak:background ratio for C Kα emission is observed with increasing current from 20 nA to 70 nA, but above ca. 70–100 nA current no improvement in signal is observed. A similar observation for optimum current and voltage conditions for C Kα measurement was made recently by Stewart (2006) for uncoated carbon-bearing metal standards in a JEOL JXA 8200 microprobe. A typical peak:background ratio for our C Kα measurement was between 13 and 15, which is about twofold improvement from the observation of Stewart (2006). Accelerating voltage of 10–13 kV was also sufficient to excite Fe and Ni Kα radiation.

3.2.2. C Kα counting time

In absence of a decontamination procedure during our probe measurement, the counting time for carbon becomes critical, as secondary carbon deposition onto the sample by prolonged beam impact may contribute to the observed signal. In order to determine the appropriate counting time for C Kα, we ran a series of tests, where we analyzed the same location of the cementite standard every 4 s up to 30 min, with repetitive peak and background counting. The peak carbon count remains more or less constant over the first 10–15 s but drops to a lower value in the next 10–20 s (Fig. 3b). After ~60 s, the count rate systematically rises (Fig. 3b). A visible mark on the surface of the standard at the point of analysis is observed at the end of the 30 min analysis cycle, clearly indicating the steady rise of count rate for C Kα after the first minute owing to progressive buildup of hydrocarbon on the surface of the standard. The background carbon count showed no variation with time. We believe that the initial reduction in peak count

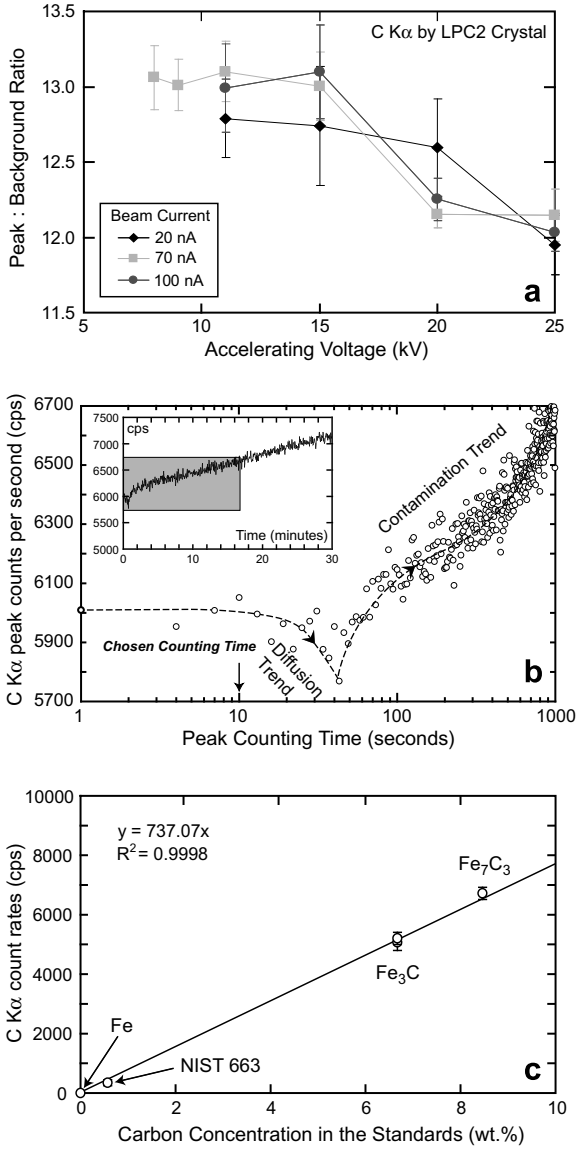

Fig. 3. Carbon analysis in metals by electron microprobe. (a) Voltage and current optimization for maximum signal to background ratio for C Kα count using Ni/C multi layer crystal in Cameca SX100 electron microprobe. The test was conducted in the synthesized Fe_3C standard and with an electron beam of 50 μm diameter. (b) A typical trend of C Kα count rates as a function of peak counting time for a 50 μm diameter electron beam with accelerating voltage of 11 kV and a beam current of 70 nA, measured on the Fe_3C standard. A steady increase of carbon count rates is observed after ~60 s, indicating build-up of secondary carbon in the form of hydrocarbon deposition at the point of electron beam impact on the sample surface. An apparent drop in count rates is also observed between ~20 and 40 s, which might be due to diffusion of carbon away from the electron beam, similar to as observed for electron probe measurement of sodium in silicate glasses (Nielsen and Sigurdsson, 1981). Peak counting time of 10 s was chosen from this observed trend, in order to avoid any possible loss or gain of carbon during the measurement. The inset shows the carbon contamination trend for up to 30 min of counting. (c) Background and blank corrected C Kα peak count rates versus known carbon concentrations in weight percents for various Fe–C standards used in this study. Count rates (counts per second) for each standard are average of more than ten measurements made on different spots on each standard using an electron beam with 11 kV accelerating voltage, 90 nA current, and a diameter of 50 μm.

rates is perhaps a result of carbon diffusion away from the beam as has been observed for sodium in glasses (Nielsen and Sigurdsson, 1981). To avoid diffusional loss of primary carbon and contamination-induced gain of secondary carbon, a short counting time of 10 s for the peak and 5 s for each background is chosen.

3.2.3. Analytical routine

Even after the choice of short counting time, measurement of the Fe standard for carbon always yielded ~0.5 wt.% carbon, which was taken as the blank value for carbon in our instrument. The C Kα count rates corresponding to this blank value were measured repeatedly for every session and were subtracted from the measured count rates for every secondary standard and unknown sample. The WDS scans on both the primary cementite standard and the pure Fe standard were performed to determine the required spectral range of background scans on each side of the C Kα peak. Matrix corrections were made using the PAP ϕρz model (Pouchou and Pichoir, 1986). The blank and background corrected count rates for C Kα showed linear relationship with concentrations of carbons in the metal standards (Fig. 3c).

4. RESULTS

4.1. Phase assemblage and texture of the run products

All the runs are saturated with graphite. For pure Fe–C systems, runs at 1200 and 1250 °C produce crystalline cementite (Fe_3C), whereas at 1275 °C, it is joined by a quenched Fe–C melt. From 1300 °C, crystalline cementite phase disappears and quenched Fe–C melt coexists with graphite from 1300 to 2500 °C. For Fe–5.2 wt.% Ni bearing runs, a single carbon-bearing Fe–Ni quenched melt exists between 1600 and 2200 °C in the presence of graphite.

Quenched Fe–C and Fe–Ni–C melts produce a dendritic network, composed of blades of cementite and interstitial kamacite or taenite at temperatures at or below 1800 °C (Fig. 4). At higher temperatures, a small proportion of graphite blades join the quench assemblage (Fig. 5). To estimate the carbon content of the metallic liquid at pre-quench run conditions, broad beam analysis of the quenched melt always included the finely dispersed graphite blades throughout the charge.

4.2. Composition of the run products and melting of Fe and Fe–Ni alloy at graphite saturation

Along the 2 GPa Fe–C join, in the presence of graphite, the stable intermediate crystalline phase below 1275 °C is cementite (Fe_3C: ~6.7 wt.% C; Fig. 6). The crystalline carbide, upon melting, produces a relatively carbon-poor melt starting at 1275 °C. This indicates that the melting relation of cementite at 2 GPa is peritectic, i.e., it melts to produce a carbon-poor melt and precipitates graphite. The carbon content of the molten Fe at 1275–1300 °C is 5.6 ± 0.1 wt.% (Fig. 6 and Table 2). Between 1300 and 1700 °C, the solubility limit of carbon in molten Fe remains nearly constant. Above 1700 °C, the carbon solubility gradually increases from 5.82 ± 0.10 wt.% at 2000 °C to 7.4 ± 0.2 wt.% at 2410 °C.

The solubility limit of carbon for molten Fe–5.2 wt.% Ni alloy, over the temperature range of our experiments and within the analytical uncertainty, is similar to that of pure-Fe (Fig. 6). However, a slightly lower solubility (~0.2–0.4 wt.%) for Fe–5.2 wt.% Ni cannot be ruled out for experimental temperature range 2000–2500 °C (Table 2 and Fig. 6), which is consistent with the observed effect of Ni on carbon solubility in molten Fe at one atmosphere (Tsymbulov and Tsmekhman, 2001) and from the measurements of carbon concentration in graphite saturated Fe–10 wt.% Ni melt by Righter et al. (1997) and Holzheid and Grove (2005). Comparison of our solubility data with those from Holzheid and Grove (2005) indicates that the trend of decreasing carbon solubility with increasing Ni content of the metallic melt, as previously noted at one atmosphere (Tsymbulov and Tsmekhman, 2001), continues at higher pressures. The storage capacity of carbon in molten Fe–5.2 wt.% Ni increases from 5.4 ± 0.1 wt.% at 1600 °C to 7.0 ± 0.3 wt.% at 2400 °C.

5. DISCUSSION

5.1. High pressure phase relation of Fe–C binary—comparison with the previous studies

Our observation of a peritectic melting relation of the cementite phase at 2 GPa (Fig. 6) is broadly consistent with the topology of 5 GPa Fe–C phase diagram calculated by Wood (1993). However, in detail, the position and the shape of the graphite saturated liquidus in the Fe–C binary presented by Wood (1993) is different from our measured carbon concentration in the graphite-saturated molten Fe. For the 5 GPa phase diagram, Wood (1993) plots a higher solubility of carbon in molten Fe at temperatures above ~1650 °C (Fig. 6). At a temperature of ~2400 °C, the calculated phase diagram of Wood (1993) at 5 GPa, predicts carbon solubility of 8.75 wt.%, whereas our experiment at 2 GPa shows that it is ~7.4 ± 0.2 wt.%. One atmosphere carbon solubility estimates (by difference) of Cahil et al. (1964) (7.75 wt.% and 7.95 wt.% at 2302 and 2327 °C, respectively) and the data compiled by Shunk (1969) (7, 7.1, 7.5, and 8.2 wt.% at 2050, 2180, 2250, and 2380 °C) and Chipman (1972) are also somewhat higher than our mean carbon solubility data (Table 1). Our data are broadly in agreement with the measurements of Holzheid and Grove (2005), which estimated lower solubility of carbon in metallic Fe–Ni melt as compared to the previous one atmosphere data and those summarized by Wood (1993).

The key feature of our measured solubility of carbon in molten Fe and Fe–Ni alloy is the small temperature dependence over a wide temperature interval in the order of ~700 °C. This indicates that the population of sites available for carbon in molten Fe or Fe–5.2 wt.% Ni does not change appreciably as a function of temperature until the graphite melting point is more closely approached. Thus the structure of the liquid itself likely controls the incorporation of carbon in the metallic Fe-rich liquid. This conclusion is reminiscent of the one of Jones and Malvin (1990)

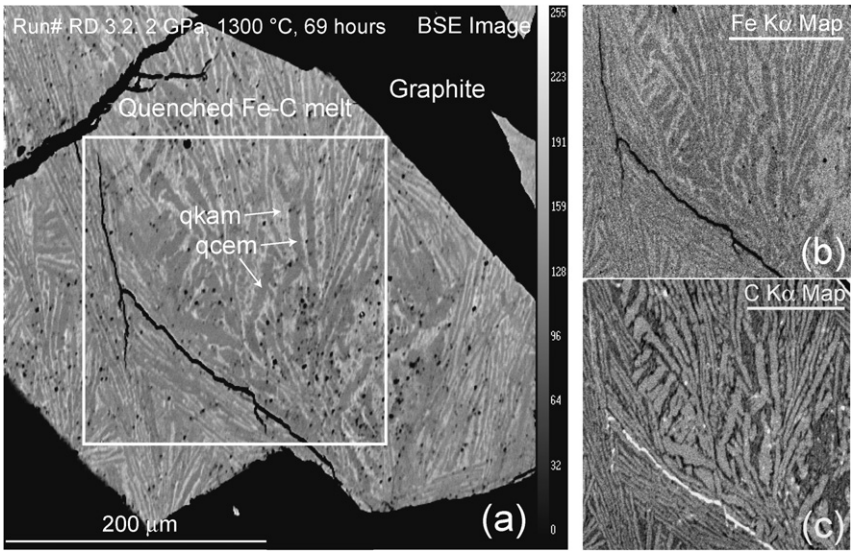

Fig. 4. (a) Backscattered electron image and (b) Fe Kα and (c) C Kα X-ray maps of a typical carbon bearing quenched Fe-melt (Run# RD 3.2: 2 GPa, 1300 °C, 69 h). The carbon bearing quenched iron melt at temperatures below 1700 °C is composed of blades of cementite (qcem) and interstitial kamacite (qkam).

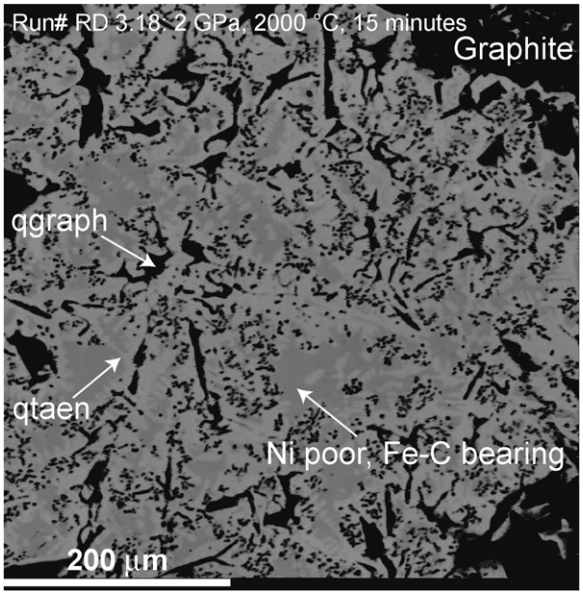

Fig. 5. Backscattered electron image of a quenched Fe–Ni–C melt from the experiment RD 3.18 (2 GPa, 2000 °C, 15 min). The quench phases comprise taenite (qtaen), a fine mixture of quenched cemenite and kamacite, and graphite (qgraph).

that liquid chemistry is more important as a determinant of partitioning behavior than temperature in Fe–Ni–S and Fe–Ni–P. The insight on which the Jones and Malvin (1990) formulation is based is that Fe-based liquids have a simple structure whose most important parameter is the population of sites available for occupation by non-metals and other ingredients. If there are no thermal speciation reactions in play to change site availability with temperature over this long temperature interval, then carbon solubility is expected to be temperature insensitive at the low temperature end, i.e., between 1300 and 2000 °C. Temperature-dependent solution models as applied by Wood (1993) may not entirely capture the interaction of carbon and Fe in the Fe-rich liquid at graphite saturation.

The difference in the shape of our solubility curve with respect to the 1 atmosphere determinations (Shunk, 1969; Chipman, 1972) may lead one to speculate that our temperature-independent results might be an artifact of quenching. If the Fe–C liquid in our experiments was unable to retain C in solution until some closure temperature were reached during the temperature–time trajectory of quenching, then quenching from a series of temperature above the closure temperature might give the appearance of uniform composition results over that temperature range. This uniformity then would only reflect the saturation value for carbon in the neighborhood of the closure temperature, not the solubility as a function of temperature. If this is the case then the closure temperature must be inferred to be 1300 °C or below for our results. But then it becomes difficult to understand why our compositions show significant variation with quenching temperature above 2000 °C. Work on the solution of oxygen in Fe provides an example of the expected results of experiments that may have had quenching effects over the temperature range of our Fe–C study. O'Neill et al. (1998) reconstructed metal solution composition for liquids saturated with magnesiowustite quenched from very high temperature and pressure, largely in the system Fe–Mg–O. They (O'Neill et al., 1998) recognized that exsolution of oxide blebs compromised the direct measurement of quenched metal compositions, and so they integrated measured blebs back into the metal compositions to determine the liquid composition at the pressure and temperature of interest. Fig. 7 shows the reconstructed oxide-saturated weight % oxygen in solution as a function of temperature for liquids quenched from 5 to 9 GPa reported by O'Neill et al. (1998). Oxygen content increases rapidly from 1800

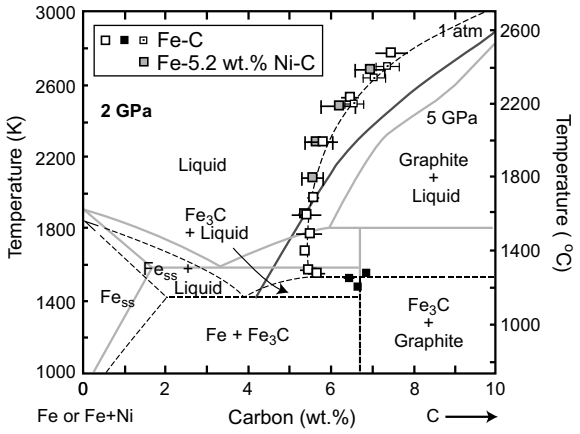

Fig. 6. Iron-rich side of the 2 GPa Fe–C binary and Fe–5.2 wt.% Ni–C pseudo binary constructed based on the graphite-saturated mineral and melt compositions from this study and previous experimental studies (Hirayama et al., 1993; Wood, 1993) and thermodynamic calculation (Wood, 1993) on the Fe–C system. The data from this study are in black squares (crystals), white squares (melts in Fe–C system), and gray squares (melts in Fe–5.2 wt.% Ni–C system) (Table 1). The smaller white squares, with black dots at the center, represent runs performed in high-temperature piston cylinder assembly with MgO insulator sleeve (Fig. 1d) and likely provide a better estimate of carbon solubility in molten Fe, due to more rapid quench in this assembly. The crystal data point at 1200 °C was a synthesis run and included in Table 2. The 2 GPa graphite saturated liquidus in black dashed line is hand drawn and not rigorously fitted. The error bars in carbon concentration for each run is the standard error of the mean based on replicate analysis ($\sigma_M = \sigma/\sqrt{n}$) and do not reflect the error owing to a finite blank value of carbon (~0.5 wt.%) in the electron probe measurements. The location of Fe–Fe_3C eutectic is based on the extrapolation from the 4–12 GPa data of the same from Hirayama et al. (1993). Also shown for comparison, are the predicted 5 GPa phase relations (in light gray) from Wood (1993) and 1 atmosphere graphite saturated liquidus (in dark gray) from Chipman (1972). Carbon solubility (2 GPa) in molten Fe or Fe–Ni alloy of core composition, at temperatures between 2000 and 2500 °C, is ~2–2.5 wt.% lower than that predicted by Wood (1993) at similar pressures.

to 2200 °C, but increases no further in the 2400 °C quenched liquid. This pattern suggests the closure temperature for oxygen in Fe liquid solutions is in the neighborhood of 2200 °C for solid media quenching trajectories. The characteristic pattern indicating this interpretation is that the solubility increases with quenching temperature and then appears to go no higher with increasing quenching temperature. This is the reverse of the pattern we see in the present experiments also shown in Fig. 7. Carbon solubility remains almost constant for quenching T up to ~2000 °C and then begins to increase. The topology is not consistent with one expected for artifacts of quenching to a closure temperature. Furthermore, the experiments run in the assembly shown in Fig. 1d giving a quicker quench are not measurably different from those run with $LaCrO_3$ insulation that provides a slower quench but better equipment service life at the highest temperatures. This also suggests that quenching artifacts are not a major feature of this data set.

The solubility of carbon only reaches on the order of 10–12% at 3100 K (Cahil et al., 1964). The melting point of graphite is poorly known but is only a few hundred degrees higher. The shape of the graphite saturated liquidus over the large stretches of composition space from 5–10 wt.% C to pure C is unexplored. But it is difficult to see how it could possibly resemble one governed by freezing point depression. Phase relations involving a solvus, metastable or otherwise, are more plausible. Thus, we believe the solubility of C in liquid Fe is more readily understood through exsolution than through solution models. The low temperature limbs of a solvus can be quite temperature insensitive. The solvus in Fe–O provides an example of this behavior that may apply to Fe–C, more at high pressure than conventional values of C solubility at 1 bar would suggest (Cahil et al., 1964; Shunk, 1969; Chipman, 1972).

5.2. Carbon solubility in core melts—the effects of pressure, temperature, and composition

In the following section we use our measured carbon solubility data to comment on the possible partitioning behavior of C between molten silicate and metal. We have used the carbon solubility limit of 6.5 wt.% for further modeling purpose. This value corresponds to our measured C solubility at 2250 °C and 2 GPa. Higher equilibration temperature, of course will lower the lower limit of $D_C^{silicate/metal}$ for any given bulk Earth carbon (Fig. 7b), but it is also necessary to evaluate whether other intensive variables can exert strong control on carbon solubility in molten metals. Here we argue that temperature is likely to be the dominant determinant of carbon solubility in Fe-rich metal melt and not pressure. The effect of pressure on carbon solubility of metal is poorly constrained. But the prediction of Wood (1993) indicates only a modest increase of carbon solubility from 7.75 wt.% at one atmosphere to ~9 wt.% to 15 GPa, through ~8.5 wt.% at 5 GPa at 2250 °C. Moreover, Wood (1993) also showed that the partial molar volume of carbon in liquid Fe–C is closer to that of diamond than graphite. Thus, the solubility of carbon in liquid Fe should remain approximately constant once the diamond field is reached. No definite pressure dependence to carbon solubility in molten metallic alloy is apparent from the study of Righter and Drake (2000), as their measured carbon concentrations at 1700 °C are 2 wt.% at 1 GPa, 1.7 wt.% at 2 and 4 GPa, and 2.3 wt.% at 6 GPa. Similarly, Holzheid and Grove (2005) also did not notice any observable pressure effect on the carbon solubility in metallic Fe–Ni melt and concluded that chemistry has more leverage in controlling the solubility of carbon in metallic liquid than pressure. Although more systematic study on the effect of pressure on carbon solubility is required, the existing studies indicate that pressure may not provide the strongest control on carbon solubility in Fe-rich molten metal. We have demonstrated that the estimated core concentration of Ni has limited effect on the solubility of carbon in molten Fe, but the presence of other possible light elements in the core melts also may influence the carbon solubility. One atmosphere data on the effect of sulfur on carbon solubility in molten Fe (Wang et al., 1991) shows ~0.5 wt.% lower

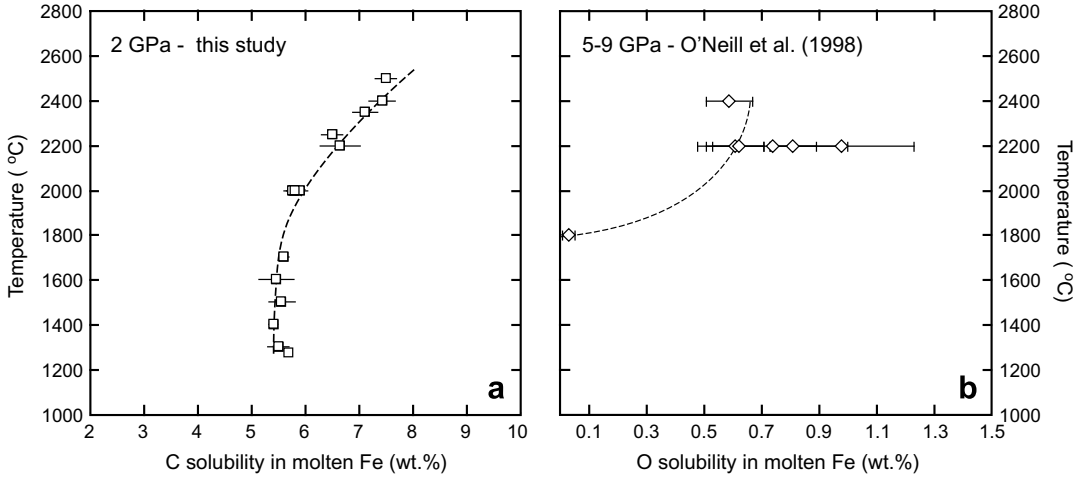

Fig. 7. Comparison of experimentally determined solubility of carbon ((a) 2 GPa—this study) and oxygen ((b) 5–9 GPa—O'Neill et al., 1998) in molten Fe as a function of temperature. The temperature dependence of solubility for oxygen as determined by O'Neill et al. (1998) is more likely to be a result of quench modification, where the dissolved oxygen in solution is blocked at a closure temperature ca. 2200 °C. Whereas our determination of carbon solubility increases with temperature above 2000 °C, making it less likely to be affected by blockage at a closure temperature. The error bar in each carbon analysis in our study is plotted as standard error of the mean and that in the study of O'Neill et al. (1998) as standard deviation.

carbon content for molten iron with ca. 2 wt.% sulfur. If the trend of decreasing C solubility with increasing S remains similar at higher pressures, carbon solubility in core melts with ~2 wt.% S (McDonough, 2003) may be ~0.5 wt.% lower than that in pure Fe or $Fe_{95}Ni_5$ as determined in this study. Thus the presence of sulfur likely offsets any positive pressure dependence of metal melt carbon solubility (Wood, 1993), lending confidence to our choice of 6–7 wt.% C as the solubility value in molten core metal.

5.3. Relative distribution of carbon between the mantle and the core

Based on the abundance of carbon in CI carbonaceous chondrite (3.2–3.5 wt.%: Anders and Grevesse, 1989; Palme and Jones, 2003) and the expected loss owing to its volatility, Earth's magma ocean was likely to be undersaturated in carbon, as at high P–T molten metal can dissolve more carbon than the concentration in the bulk protoearth (Wang et al., 1991; Wood, 1993; Righter et al., 1997; Righter and Drake, 2000; this study). Thus our experiments only provide a maximum limit of the carbon concentration in planetary metallic core that inherits its chemical signature from a shallow, carbon-undersaturated magma ocean. The actual carbon budget of the Earth's core and the residual mantle was likely set by equilibrium partitioning between the silicate and metallic melts, $D_C^{silicate/metal}$. Experimental determination of a carbon partition coefficient between immiscible silicate melt and metallic melt is lacking. But the carbon solubility data in core melts and the knowledge of the observed concentration of carbon in the present day Earth's mantle can provide us constraints on the likely partitioning behavior of carbon between the silicate mantle and the metallic core, assuming that the carbon presently in the mantle was set through equilibrium with the core.

5.3.1. Constraints on carbon partitioning from the carbon solubility in core melts

Assuming the core of Earth to be a ~1/3 equilibrium melt derived from the protoearth (the mass of the Earth's core is 32.3% of the planet) and assuming all C dissolves in either the metallic core or the silicate Earth, we calculated the concentration of carbon in the metallic core melts, C_C^{metal}, for a range of plausible $D_C^{silicate/metal}$ and for a range of initial carbon content, C_C^0, from chondritic (3.2–3.5 wt.%: Anders and Grevesse, 1989; Palme and Jones, 2003) to sub-chondritic values (Fig. 8a), following the equation—

$$C_C^{metal} = \frac{C_C^0}{D_C^{silicate/metal} + 0.323(1 - D_C^{silicate/metal})} \quad (1)$$

Comparison of the solubility limit of C derived from our experiments with that of our model curves for C_C^{metal} constrains the lower limit of $D_C^{silicate/metal}$ for chondritic or near-chondritic carbon concentrations (Fig. 8b). However, for carbon content of the source <~2 wt.%, the model carbon content in the metallic melts fall below our solubility limit for any values of $D_C^{silicate/metal}$ (Fig. 8a). Thus the lower limit of $D_C^{silicate/metal}$ cannot be constrained solely from our carbon solubility data for low bulk Earth carbon content (Fig. 8b).

5.3.2. Constraints on carbon partitioning from the concentration of carbon in the silicate Earth

The immiscible silicate melt left behind after the segregation of the core largely forms the Earth's mantle. Thus the observed carbon concentration of the present day mantle should indicate the concentration of the carbon in the silicate residual to core separation if no further process alters its carbon content. We recognize two main processes that may influence the carbon content of the residual silicate—the first is the addition of carbon by late veneer, C_C^{veneer}

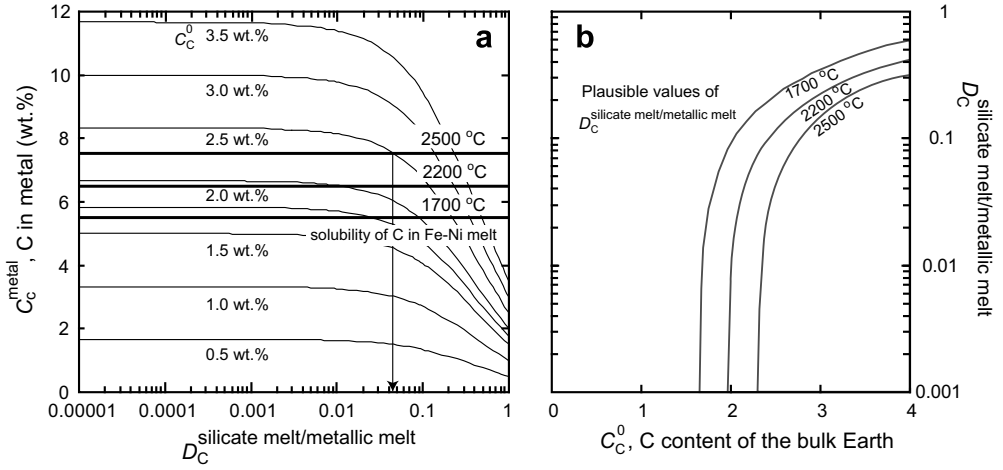

Fig. 8. (a) Concentrations of carbon in the metallic core melt, C_C^{metal} as a function of partition coefficient of carbon between silicate melt and metallic melt, $D_C^{silicate/metal}$ where the core has been modeled as 32.3% equilibrium batch melts of the protoearth. Model carbon contents for the core are plotted for initial bulk Earth carbon contents, C_C^0 varying from chondritic (~3.5 wt.%) to subchondritic values. Superimposed on the model curves are the carbon solubility limits at 1700, 2200, and 2500 °C derived from our 2 GPa experiments. The intersection between the solubility limit at any given temperature and the model curve for a given C_C^0, constrains the lower limit of $D_C^{silicate/metal}$. For example, the lowest possible value of $D_C^{silicate/metal}$ for bulk Earth carbon of 2.5 wt.% and for a magma ocean temperature of 2500 °C is ~0.043, as pointed by the down arrow. (b) The plausible values of $D_C^{silicate/metal}$ as a function of bulk Earth carbon content, C_C^0 derived from the comparison in the left panel (a). The curves for each temperature mark the lower bound of $D_C^{silicate/metal}$ for any given C_C^0.

and the second an internal differentiation of bulk silicate Earth carbon, $C_C^{silicate}$ between the mantle, C_C^{mantle} and the crust, C_C^{crust}. We estimated the bulk silicate Earth carbon, that is residual to core separation, $C_C^{silicate}$ by the expression $C_C^{silicate} = (C_C^{mantle} \times M^{mantle} + C_C^{crust} \times M^{crust} - C_C^{veneer} \times M^{veneer})/M^{silicate}$, where C and M represent concentration and mass, respectively. Assuming an average C_C^{mantle}, C_C^{crust}, and C_C^{veneer} in the order ~225 ppm [assuming that the mantle comprises ~40% by mass of DMM-like reservoir (Workman and Hart, 2005) with an average C content of ~30 ppm (Marty and Tolstikhin, 1998) and the rest is an enriched reservoir with an average C content of ~350 ppm (Dixon et al., 1997)], 7000 ppm (Javoy et al., 1982; Hayes and Waldbauer, 2006), and 35,000 ppm (veneer of CI carbonaceous chondrite: Anders and Grevesse, 1989) and mass of the 'late veneer' being 0.5% of that of the mantle (e.g., Wood et al., 2006), we get $C_C^{silicate}$ of ~100 ppm. This estimate of residual silicate carbon, by taking into account a possible late addition of carbon by a late chondritic veneer, is consistent with the model proposed by Javoy (1997) and is well within the range of estimates for the present day mantle (30–1100 ppm) as derived from the observed CO_2 content of the mid-ocean ridge and ocean island basalts (Javoy and Pineau, 1991; Dixon et al., 1997; Marty and Tolstikhin, 1998; Saal et al., 2002; Pineau et al., 2004). Thus, hereafter, we use the range of carbon content of the mantle for our reference value of $C_C^{silicate}$ ($C_C^{silicate} \approx C_C^{mantle}$). We independently calculated the carbon concentration in the silicate melt residue resulting from core segregation, $C_C^{silicate}$ for a range of plausible $D_C^{silicate/metal}$ and for a range of initial carbon contents, C_C^0, from chondritic (3.2–3.5 wt.%: (Anders and Grevesse, 1989; Palme and Jones, 2003) to sub-chondritic values based on equilibrium (Eq. (2), Fig. 9a) and fractional segregation of core melts (Eq. (3), Fig. 9c).

$$C_C^{silicate} = \frac{C_C^0 \times D_C^{silicate/metal}}{D_C^{silicate/metal} + 0.323(1 - D_C^{silicate/metal})} \quad (2)$$

$$C_C^{silicate} = C_C^0(1 - 0.323)^{\left(\frac{1}{D_C^{silicate/metal}} - 1\right)} \quad (3)$$

Comparison of the model curves with the observed mantle carbon content and translation of the limits of $D_C^{silicate/metal}$ derived from our solubility data shows that the carbon concentration of the residual silicate cannot be matched by the process of shallow magma ocean fractionation of carbon between metal and silicate in a chondritic or near-chondritic protoearth (Fig. 9a and c). This may indicate the presence of a hidden carbon-rich mantle reservoir untapped by oceanic volcanism, which may not be totally implausible as recent findings indicate the existence of deep Earth reservoir with higher than background carbon content (Brenker et al., 2007) indicating heterogeneous distribution of carbon in the Earth's mantle. Perhaps a more likely scenario, however, is volatility-driven loss of carbon during accretion to bring the bulk Earth concentration down to sub-chondritic value (Wood, 1993). Indeed the bulk Earth carbon concentration estimate is at least an order of magnitude lower than that of chondrite (730–1000 ppm: Marty and Jambon, 1987; McDonough, 2003), barring the uncertainty in the behavior of carbon during Earth's accretion (Wood, 1993). For bulk Earth carbon <1–2 wt.% and for carbon solubility in core melts in the order of 6–7 wt.%, the entire range of mantle carbon concentration from enriched to depleted reservoir can be matched for both equilibrium and fractional segregation of core melts (Fig. 9a and c).

We also constrained the partition coefficient of carbon between the silicate and the metal, $D_C^{silicate/metal}$ independently from the knowledge of carbon content of the bulk

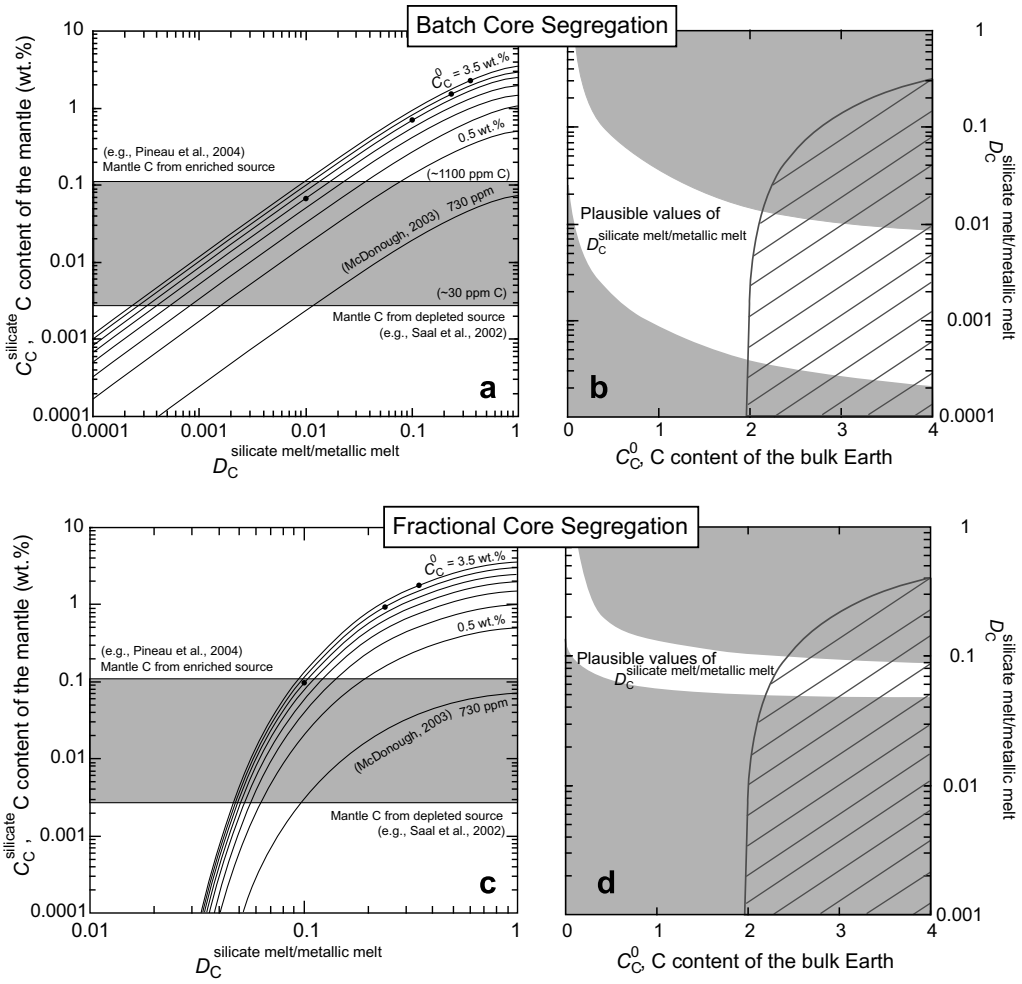

Fig. 9. Left panels: concentrations of carbon in the mantle, based on equilibrium batch segregation (a) and fractional segregation (c) of core melts as a function of partition coefficient of carbon between silicate melts and metallic core melts, $D_C^{silicate/metal}$. Model carbon contents for the silicate residue are shown for bulk Earth carbon contents, C_C^0 varying from chondritic (~3.5 wt.%) to subchondritic values. Superimposed on the model curves are the mantle carbon estimates based on the concentration of carbon in the oceanic basalts. The lower limit of the gray band indicates carbon content of a depleted mantle reservoir whereas the upper limit marks the estimate for an enriched mantle reservoir. The intersection between the model curves with that of an estimated mantle carbon value constrains the partition coefficient of carbon between silicate melt and metallic core melt, $D_C^{silicate/metal}$. Because of the uncertainty in the average mantle carbon content, we prefer to note an upper (assuming whole mantle carbon content of ~1100 ppm) and lower bound (assuming whole mantle carbon content of ~50 ppm) of $D_C^{silicate/metal}$ for any C_C^0 value of interest. Also shown for each curve is the lower limit of $D_C^{silicate/metal}$ as derived from the carbon solubility data in core melts (black dots), which indicates that the observed concentration of carbon in the mantle cannot be matched by partitioning of carbon for a chondritic protoearth. The absence of constraints on minimum $D_C^{silicate/metal}$ for any curve indicates that the minimum $D_C^{silicate/metal}$ is not constrained for those particular bulk compositions from the carbon solubility in the metallic melts. Right panels: constraints on $D_C^{silicate/metal}$ based on equilibrium batch segregation (b) and fractional segregation (d) of core melts and observed carbon concentration in the present day mantle in the C_C^0 versus $D_C^{silicate/metal}$ space. The white fields delimit the plausible values of $D_C^{silicate/metal}$. Also superimposed is the region of $D_C^{silicate/metal}$ versus C_C^0 that is not permitted by the carbon solubility in core melts assuming a magma ocean temperature of ~2500 K (hatched field).

silicate Earth or the mantle, $C_C^{silicate}$ and by calculating $C_C^{silicate}$ that results from removal of 32.3% metallic core melt by batch or fractional process (Fig. 9b and d). In fact, by this procedure we can constrain, for any given bulk Earth carbon, both the lower bound as well as the upper bound of $D_C^{silicate/metal}$ from the most depleted and enriched mantle end-members for carbon, respectively (Fig. 9b and d). If the depleted mantle carbon concentration (~30 ppm) is applied to the whole mantle and segregation of core melts was by an equilibrium or batch process then the $D_C^{silicate/metal}$ varies between 0.01 and 0.0002 for bulk Earth carbon varying between <0.1 wt.% to 3.5 wt.%; whereas if we apply the enriched mantle carbon content (~1000 ppm) to the entire mass of the mantle then the $D_C^{silicate/metal}$ varies between values >1 and ~0.01 (Fig. 9b). A similar calculation for core separation by purely fractional melt segregation process produces $D_C^{silicate/metal}$ between 0.1–0.05 and 1.0–0.09 for depleted and enriched mantle carbon, respectively, and for bulk Earth carbon varying between ~0.1 and 3.5 wt.% (Fig. 9d).

The most complete constraints of $D_C^{silicate/metal}$ come from combining the constraints derived from our solubility data and that derived from the estimate of the present day mantle concentration. Fig. 9b and d shows the feasible solution for the C_C^0 versus $D_C^{silicate/metal}$ space for core segregation by equilibrium and fractional process. The plausible values of $D_C^{silicate/metal}$ varies between ~0.0004–0.01 and 0.01–1.0 for equilibrium core melt extraction and between 0.05–0.1 and 0.1–1.0 for fractional extraction of core melts.

5.4. Carbon in the core?

The trend of carbon solubility versus temperature from our experiments indicates that concentration approaching the solubility limit and a magma ocean temperature in excess of 3000 K are required for carbon to be the sole light element in the Earth's outer core. Although the expected magma ocean adiabat may allow temperature approaching or even in excess of 3000 K (Wood et al., 2006), our estimated range of possible $D_C^{silicate/metal}$ indicates that metallic liquid will achieve carbon concentration of ~10 wt.% only if chondritic value carbon content applies for bulk Earth (Fig. 10). However, satisfying both the observed carbon content of the bulk silicate Earth and the core melt solubility corresponding to magma ocean temperature of ~2200 °C precludes bulk Earth carbon content greater than 2 wt.%, unless there is free carbide or graphite in the core. We estimate the carbon content of the bulk metallic core at a maximum of ~6 wt.% for bulk Earth carbon of ~2 wt.% and as low as 0.1–0.4 wt.% for bulk Earth carbon of ~0.1 wt.% (Fig. 10). We note that this estimate of carbon content pertains to the bulk core melt that segregates from the silicate and does not apply strictly to the carbon content for the Earth's liquid outer core. Crystallization of the inner core likely influences the light element budget of the outer core, but its effect on the carbon content of the outer core is likely to be minimal. If the Fe–Fe_3C eutectic composition, which is ~4 wt.% carbon at 1 atmosphere, is insensitive to pressure (Hirayama et al., 1993; Fei et al., 2007), a metallic core melt with 0.1–0.4 wt.% carbon likely crystallizes a nominally carbon-free Fe(–Ni) metal. However, if the Fe–Fe_3C eutectic composition shifts to lower carbon content with increasing pressure (Wood, 1993) then a metallic core melt with only 0.1–0.4 wt.% carbon may also crystallize an iron carbide phase. In the former case, crystallization of 5% by mass of pure Fe(–Ni) inner core would only raise the carbon budget of the outer core by 5%, i.e., 0.11–0.42 wt.% for bulk Earth carbon of ~0.1 wt.%. If the latter case is more appropriate, crystallization of 5% Fe_3C or perhaps Fe_7C_3 inner core would lower the carbon content of the outer core by a negligible amount. Our estimate of carbon concentration in the core is in agreement with the recent mass balance argument for 0.2 wt.% carbon in the core (McDonough, 2003).

Based on our estimate, the core is likely one of the most enriched terrestrial reservoirs of carbon with concentration as high as 4000 ppm, which likely is at least an order of magnitude higher than that of the average mantle. Also in terms of the total mass, Earth's core likely stores $\sim(48 \pm 29) \times 10^{23}$ g C, which is higher than the current estimate of carbon in the mantle.

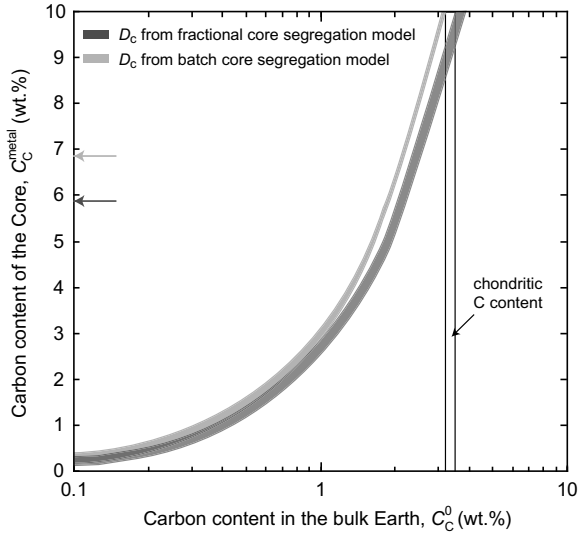

Fig. 10. Concentration of carbon in the core as a function of bulk Earth carbon content with constraints for $D_C^{silicate/metal}$ derived from our carbon solubility data and the concentration of carbon in the mantle. Maximum average possible values for core carbon content (6–7 wt.%), which satisfies both the carbon content of the present day mantle and the carbon solubility in core melts at ~2500 K, for batch and fractional core segregation models are marked by light gray and dark gray arrows, respectively. However, a more realistic value for carbon content in the core is 0.1–0.4 wt.%, a value corresponding to a bulk Earth carbon content of ~0.1 wt.%.

6. CONCLUDING REMARKS

Our experimental carbon solubility data for molten iron at 2 GPa and to 2500 °C is lower than the summary of Wood (1993) at similar pressures. We also find that up to 5.2 wt.% Ni has limited influence on carbon solubility in core melts. Carbon solubility in molten Fe–Ni alloy with ~5 wt.% Ni is 0.2–0.3 wt.% lower than that in pure Fe melt. Comparison of our carbon solubility data in core melts and present day estimate of mantle carbon with the core-mantle equilibration models between segregating metallic liquid and silicate melt constrain the partition coefficient for carbon between core and the mantle. We infer that if a chondritic concentration for carbon of ~3.5 wt.% is assumed for bulk Earth, then Earth's mantle likely has a carbon rich reservoir untapped by oceanic volcanism. However, if accretionary loss of carbon brings down the bulk Earth carbon to only ~1000 ppm then the present day mantle carbon concentration can be explained by equilibrium between metal and silicate in a hot magma ocean with carbon concentration of 0.25 ± 0.15 wt.% in the core. This indicates that carbon is unlikely to account for the observed 5–10% density deficit of Earth's outer core with respect to molten Fe–Ni alloy (Birch, 1964; Anderson and Isaak, 2002).

Future studies on direct measurement of carbon partition coefficient at magma ocean conditions would be required to further the understanding of carbon distribution between planetary mantle and core. The equilibrium

partition coefficient for carbon is likely to be a function of pressure, temperature, and oxygen fugacity as these intensive variables influence the speciation of carbon in silicate melt (Nowak et al., 2003; Kadik et al., 2004). The balance of carbon bearing volatile species of interest in magma ocean silicate melt is largely unknown based on our present state of the knowledge. But our mass balance approach provides the most complete range of possibilities for carbon partitioning—this range actually puts constraints on possible conditions of metal–silicate equilibration and speciation of volatiles in melts. Comparison of experimentally determined carbon partition coefficients under various P–T–fO_2 conditions in the future with the framework for range of $D_C^{silicate/metal}$ presented here will help constrain the conditions of metal–silicate equilibration in a magma ocean. But in any case, the core is likely to be the most enriched reservoir of carbon in the Earth's interior and likely stores the largest mass of terrestrial carbon.

ACKNOWLEDGMENTS

We are grateful to Nancy Chabot, Heather Watson, and an anonymous reviewer for providing supportive formal reviews. We also appreciate informal and supportive comments by John Longhi and Wim van Westrenen and discussion with Mike Walter and Elizabeth Cottrell. We are grateful to Charlie Mandeville for help with the electron microprobe measurement and to George Harlow for help with the XRD. R.D. acknowledges helpful discussion with Bill McDonough on modeling core composition and Wim van Westrenen for drawing attention to the Ph.D. thesis chapter of Andrew Stewart on carbon measurement in metals by electron microprobe. R.D. acknowledges post-doctoral research fellowship from Lamont-Doherty Earth Observatory of Columbia University. This work was supported by the NSF and is LDEO contribution #7182.

REFERENCES

Anders E. and Grevesse N. (1989) Abundances of the elements: meteoritic and solar. *Geochim. Cosmochim. Acta* **53**, 197–214.

Anderson O. L. and Isaak D. G. (2002) Another look at the core density deficit of Earth's outer core. *Phys. Earth Planet. Int.* **131**, 19–27.

Bastin G. F. and Heijligers H. J. M. (1986) Quantitative electron probe microanalysis of carbon in binary carbides. I—principles and procedures. *X-Ray Spectrom.* **15**, 135–141.

Berner R. A. (1999) A new look at the long-term carbon cycle. *GSA Today* **9**, 1–6.

Birch F. (1964) Density and composition of mantle and core. *J. Geophys. Res.* **69**, 4377–4388.

Blundy J. D. and Dalton J. (2000) Experimental comparison of trace element partitioning between clinopyroxene and melt in carbonate and silicate systems, and implications for mantle metasomatism. *Contrib. Miner. Petrol.* **139**, 356–371.

Bourgue E. and Richet P. (2001) The effects of dissolved CO_2 on the density and viscosity of silicate melts: a preliminary study. *Earth Planet. Sci. Lett.* **193**, 57–68.

Brenker F. E., Vollmer C., Vincze S., Vekemans B., Szymanski A., Janssens K., Szaloki I., Nasdala L., Joswig W. and Kaminsky F. (2007) Carbonates from lower part of transition zone or even the lower mantle. *Earth Planet. Sci. Lett.*

Cahil J. A., Kirshenbaum A. D. and Grosse A. V. (1964) The solubility of carbon in liquid iron to 3160 K and viscosity estimates of Fe–C solutions to 2500 K. *Trans. Am. Soc. Metals* **57**, 417–426.

Chabot N. L. and Agee C. B. (2003) Core formation in the Earth and Moon: new experimental constraints from V, Cr, and Mn. *Geochim. Cosmochim. Acta* **67**, 2077–2091.

Chabot N. L., Campbell A. J., Jones J. H., Humayoun M. and Vern Lauer H. J. (2006) The influence of carbon on trace element partitioning behavior. *Geochim. Cosmochim. Acta* **70**, 1322–1335.

Chabot N. L., Draper D. S. and Agee C. B. (2005) Conditions of core formation in the Earth: constraints from nickel and cobalt partitioning. *Geochim. Cosmochim. Acta* **69**, 2141–2151.

Chipman J. (1972) Thermodynamics and phase diagram of the Fe–C system. *Metall. Trans.* **3**, 55–64.

Coltice N., Simon L. and Lecuyer C. (2004) Carbon isotope cycle and mantle structure. *Geophys. Res. Lett.* **31**, L05603. doi:10.1029/2003GL018873.

Cottrell E. and Walker D. (2006) Constraints on core formation from Pt partitioning in mafic silicate liquids at high temperatures. *Geochim. Cosmochim. Acta* **70**, 1565–1580.

Dasgupta R. and Hirschmann M. M. (2006) Melting in the Earth's deep upper mantle caused by carbon dioxide. *Nature* **440**, 659–662.

Dixon J. E., Clague D. A., Wallace P. and Poreda R. (1997) Volatiles in alkalic basalts from the north arch volcanic field, Hawaii: extensive degassing of deep submarine-erupted alkalic series lavas. *J. Petrol.* **38**, 911–939.

Dobson D. P. and Wiedenbeck M. (2002) Fe- and C-self-diffusion in liquid Fe_3C to 15 GPa. *Geophys. Res. Lett.* **29**. doi:10.1029/2002GL015536.

Fei Y., Wang Y. and Deng L. (2007) Melting relations in the Fe–C–S system at high pressure: implications for the chemistry of the cores of the terrestrial planets. *Lunar and Planetary Science XXXVIII*. Houston, TX, USA.

Fram M. S. and Longhi J. (1992) Phase equilibria of dikes associated with Proterozoic anorthosite complexes. *Am. Miner.* **77**, 605–616.

Hayes J. F. and Waldbauer J. R. (2006) The carbon cycle and associated redox processes through time. *Philos. Trans. R. Soc. Lond.* **B361**, 931–950.

Hillgren V. J., Gessmann C. K. and Li J. (2000) An experimental perspective on the light element in Earth's core. In *Origin of the Earth and Moon* (eds. R. M. Canup and K. Righter). The University of Arizona Press, Tucson.

Hirayama Y., Fujii T. and Kurita K. (1993) The melting relation of the system, iron and carbon at high pressure and its bearing on the early stage of the Earth. *Geophys. Res. Lett.* **20**, 2095–2098.

Holzheid A. and Grove T. L. (2005) The effect of metal composition on Fe–Ni partition behavior between olivine and FeNi–metal, FeNi–carbide, FeNi–sulfide at elevated pressure. *Chem. Geol.* **221**, 207–224.

Huang L., Skorodumova N. V., Belonoshko A. B., Johansson B. and Ahuja R. (2005) Carbon in iron phases under high pressure. *Geophys. Res. Lett.* **32**, L21314.

Hunter R. H. and McKenzie D. (1989) The equilibrium geometry of carbonate melts in rocks of mantle composition. *Earth Planet. Sci. Lett.* **92**, 347–356.

Jana D. and Walker D. (1997) The impact of carbon in element distribution during core formation. *Geochim. Cosmochim. Acta* **61**, 2759–2763.

Jana D. and Walker D. (1999) Core formation in the presence of various C–H–O volatile species. *Geochim. Cosmochim. Acta* **63**, 2299–2310.

Javoy M. (1997) The major volatile elements of the Earth: their origin, behavior, and fate. *Geophys. Res. Lett.* **24**, 177–180.

Javoy M. and Pineau F. (1991) The volatiles record of a 'popping' rock from the Mid-Atlantic Ridge at 14°N: chemical and isotopic composition of gas trapped in the vesicles. *Earth Planet. Sci. Lett.* **107**, 598–611.

Javoy M., Pineau F. and Allègre C. J. (1982) Carbon geodynamic cycle. *Nature* **300**, 171–173.

Jones J. H. and Malvin D. J. (1990) A nonmetal interaction model for the segregation of trace metals during solidification of Fe–Ni–S, Fe–Ni–P, and Fe–Ni–S–P alloys. *Metall. Mater. Trans. B* **21B**, 697–706.

Kadik A., Pineau F., Litvin Y., Jendrzejewski N., Martinez I. and Javoy M. (2004) Formation of carbon and hydrogen species in magmas at low oxygen fugacity. *J. Petrol.* **45**, 1297–1310.

Kuramoto K. (1997) Accretion, core formation, H and C evolution of the Earth and Mars. *Phys. Earth Planet Int.* **100**, 3–20.

Kuramoto K. and Matsui T. (1996) Partitioning of H and C between the mantle and core during the core formation in the Earth: its implications for the atmospheric evolution and redox state of early mantle. *J. Geophys. Res.* **101**, 14909–14932.

Lange R. A. (1994) The effect of H_2O, CO_2, and F on the density and viscosity of silicate melts. In *Volatiles in Magmas* (eds. M. R. Carroll and J. R. Holloway). Mineralogical Society of America, Washington, DC.

Li J. and Agee C. B. (1996) Geochemistry of mantle-core differentiation at high pressure. *Nature* **381**, 686–689.

Li J. and Agee C. B. (2001a) The effect of pressure, temperature, oxygen fugacity and composition on partitioning of nickel and cobalt between liquid Fe–Ni–S alloy and liquid silicate: Implications for the Earth's core formation. *Geochim. Cosmochim. Acta* **65**, 1821–1832.

Li J. and Agee C. B. (2001b) Element partitioning constraints on the light element composition of the Earth's core. *Geophys. Res. Lett.* **28**, 81–84.

Li J. and Fei Y. (2003) Experimental constraints on core composition. In *The Mantle and Core* (ed. R. W. Carlson). Elsevier, Amsterdam.

Longhi J. (2005) Temporal stability and pressure calibration of barium carbonate and talc/pyrex pressure media in a piston-cylinder apparatus. *Am. Miner.* **90**, 206–218.

Marty B. and Jambon A. (1987) $C/^3He$ in volatile fluxes from the solid Earth: implications for carbon geodynamics. *Earth Planet. Sci. Lett.* **83**, 16–26.

Marty B. and Tolstikhin I. N. (1998) CO_2 fluxes from mid-ocean ridges, arcs and plumes. *Chem. Geol.* **145**, 233–248.

McDonough W. F. (2003) Compositional model for the Earth's core. In *The Mantle and Core* (ed. R. W. Carlson). Elsevier-Pergamon, Oxford.

Minarik W. G. and Watson E. B. (1995) Interconnectivity of carbonate melt at low melt fraction. *Earth Planet. Sci. Lett.* **133**, 423–437.

Nielsen C. H. and Sigurdsson H. (1981) Quantitative methods for electron microprobe analysis of sodium in natural and synthetic glasses. *Am. Miner.* **66**, 547–552.

Nowak M., Porbatzki D., Spickenbom K. and Diedrich O. (2003) Carbon dioxide speciation in silicate melts: a restart. *Earth Planet. Sci. Lett.* **207**, 131–139.

O'Neill H. S. C., Canil D. and Rubie D. C. (1998) Oxide-metal equilibria to 2500 °C and 25 GPa: implications for core formation and the light component in the Earth's core. *J. Geophys. Res.* **103**, 12239–12260.

Palme H. and Jones A. (2003) Solar system abundances of the elements. In *Meteorites, Comets, and Planets* (ed. A. M. Davis). Elsevier Ltd., Amsterdam.

Pineau F., Shilobreeva S., Hekinian R., Bidiau D. and Javoy M. (2004) Deep-sea explosive activity on the Mid-Atlantic Ridge near 34°50′N: a stable isotope (C, H, O) study. *Chem. Geol.* **211**, 159–175.

Poirier J.-P. (1994) Light elements in the Earth's outer core: a critical review. *Phys. Earth Planet. Int.* **85**, 319–337.

Pouchou J.-L. and Pichoir F. (1986) Very light elements X-ray microanalysis. Recent models of quantification. *J. de Microscopie et de Spectroscopie Electronique* **11**, 229–250.

Righter K. and Drake M. J. (2000) Metal/silicate equilibrium in the early Earth—new constraints from the volatile moderately siderophile elements Ga, Cu, P, and Sn. *Geochim. Cosmochim. Acta* **64**, 3581–3597.

Righter K., Drake M. J. and Yaxley G. (1997) Prediction of siderophile element metal–silicate partition coefficients to 20 GPa and 2800 °C: the effects of pressure, temperature, and oxygen fugacity, and silicate and metallic melt compositions. *Phys. Earth Planet. Int.* **100**, 115–134.

Righter K. and Shearer C. (2003) Magmatic fractionation of Hf and W: constraints on the timing of core formation and differentiation in the Moon and Mars. *Geochim. Cosmochim. Acta* **67**, 2497–2507.

Robaut F., Crisci A., Durand-Charre M. and Jouanne D. (2006) Practical aspects of carbon content determination in carburized steels by EPMA. *Microsc. Microanal.* **12**, 331–334.

Saal A. E., Hauri E., Langmuir C. H. and Perfit M. R. (2002) Vapour undersaturation in primitive mid-ocean-ridge basalt and the volatile content of Earth's upper mantle. *Nature* **419**, 451–455.

Shunk F. A. (1969) *Constitution of Binary Alloys, Second Supplement*. McGraw-Hill Book Company, New York.

Sleep N. H. and Zahnle K. (2001) Carbon dioxide cycling and implications for climate on ancient earth. *J. Geophys. Res.* **106**, 1373–1399.

Stewart A. J. (2006) Planetary cores: effect and behaviour of minor elements on the Fe–S system to 40 GPa. Ph.D. Disseration Number 16815, ETH Zurich, 108 pp.

Thibault Y. and Walter M. J. (1995) The influence of pressure and temperature on the metal–silicate partition coefficients of nickel and cobalt in a model C1 chondrite and implications for metal segregation in a deep magma ocean. *Geochim. Cosmochim. Acta* **59**, 991–1002.

Tsuzuki A., Sago S., Hirano S.-I. and Naka S. (1984) High temperature and pressure preparation and properties of iron carbides Fe_7C_3 and Fe_3C. *J. Mater. Sci.* **19**, 2513–2518.

Tsymbulov L. B. and Tsmekhman L. S. (2001) Solubility of carbon in sulfide melts of the system Fe–Ni–S. *Russ. J. Appl. Chem.* **74**, 925–929.

Walter M. J. and Thibault Y. (1995) Partitioning of tungsten and molybdenum between metallic liquid and silicate melt. *Science* **270**, 1186–1189.

Wang C., Hirama J., Nagasaka T. and Ban-Ya S. (1991) Phase equilibria of liquid Fe–S–C ternary system. *ISIJ Int.* **31**, 1292–1299.

Wood B. J. (1993) Carbon in the core. *Earth Planet. Sci. Lett.* **117**, 593–607.

Wood B. J., Walter M. J. and Wade J. (2006) Accretion of the Earth and segregation of its core. *Nature* **441**, 825–833.

Workman R. K. and Hart S. R. (2005) Major and trace element composition of the depleted MORB mantle (DMM). *Earth Planet. Sci. Lett.* **231**, 53–72.

Wyllie P. J. and Huang W.-L. (1975) Influence of mantle CO_2 in the generation of carbonatites and kimberlites. *Nature* **257**, 297–299.

Zhang Y. and Zindler A. (1993) Distribution and evolution of carbon and nitrogen in Earth. *Earth Planet. Sci. Lett.* **117**, 331–345.

Associate editor: F.J. Ryerson